JOURNAL OF AIRCRAFT
Vol. 46, No. 2, March–April 2009

Investigation of the Propeller Slipstream with Particle Image Velocimetry

Eric W. M. Roosenboom,* André Heider,† and Andreas Schröder‡
DLR, German Aerospace Center, 37073 Göttingen, Germany

DOI: 10.2514/1.33917

The flow around an 8-bladed propeller is analyzed using particle image velocimetry in the Airbus low-speed wind tunnel facility in Bremen, Germany. The propeller is mounted on a half-model equipped with two propellers with opposing rotation directions, where only the outboard propeller is investigated. For two cases with no thrust ($C_T = 0$) and with thrust ($C_T = 0.1$) the propeller slipstream is visualized at several angles of attack. In particular, the development of the slipstream over the wing is investigated with particle image velocimetry derived variables such as mean velocities, fluctuations, and turbulent kinetic energy. A detailed description of the slipstream returns valuable information on the vortical structures and periodic phenomena. An identification of such events is necessary for a future validation with numerical data. It allows for the analysis of parametric cases; first, a comparison between the thrust and no-thrust cases and, second, the effect of an increasing angle of attack. It is found that at the thrust cases, for higher angles of attack, vortices are formed due to interactions in the boundary layer.

Nomenclature

C_T	=	thrust coefficient, $C_T = T/q_\infty S_{\text{ref}}$
D	=	diameter
J	=	advance ratio, $J = U_\infty/n_p D$
K	=	turbulent kinetic energy
n_p	=	revolutions per second
q_∞	=	dynamic pressure
	=	propeller radius
r/R	=	normalized distance
S_{ref}	=	reference surface
T	=	thrust
u	=	velocity in x direction
u'	=	velocity fluctuation in x direction
U_∞	=	free stream velocity
v	=	velocity in y direction
v'	=	velocity fluctuation in y direction
$\|V\|$	=	magnitude of velocity, $\|V\| = \sqrt{u^2 + v^2 + w^2}$
w	=	velocity in z direction
w'	=	velocity fluctuation in z direction
x	=	longitudinal axis (of wind tunnel model)
y	=	lateral axis (of wind tunnel model)
z	=	normal axis (of wind tunnel model)
α	=	angle of attack
ω_y	=	out-of-plane component of vorticity, $\omega_y = \frac{\partial u}{\partial z} - \frac{\partial w}{\partial x}$, in wind tunnel model coordinate system

I. Introduction

IN THE first successful powered flight in aerospace history the Wright brothers used a propeller-powered aircraft in Kitty Hawk, North Carolina on 17 December 1903. The development of turboprops and other propulsive systems emerged rapidly thereafter. However, the development of turboprops designed for high(er) cruise speeds suffered from problems related to these complex systems, such as blade dynamic behavior and fatigue. During the last decade oil prices have continuously increased, and so knowledge of propeller phenomena is of interest again. Advanced turboprops have a significant (10–30%) larger propulsive efficiency at (slightly) lower operating cruise speeds, when compared with turbojets and high bypass turbofans [1,2]. The speed disadvantage is of no influence on regional flights. In fact, at slightly lower speeds than the maximum cruise speed turboprops have a longer range and endurance. Moreover, there are environmental and economical benefits. Because of the higher propulsive efficiency less fuel is consumed, leading to less pollution, and, although not directly noticeable in the direct operating costs, at high oil prices fewer costs are related to fuel [2]. The favorable propulsive efficiency of turboprops also has its advantage on take-off and landing performance, and combined with their long endurance makes them explicitly useful for military tasks, such as steep descents, takeoffs from short or ruined runways, surveillance, cargo droppings, and other tactical missions.

In current times where one has to seriously keep in mind the supply of fossil fuels, turboprops, with their low fuel consumption, are once again considered as competitive alternatives for the propulsion of airplanes. One major drawback of the lack of interest in propeller research is the limited availability of experimental results. Progress has been made in naval research, but marine propeller investigations focus mainly on naval phenomena and most investigations are performed in cavitation tunnels [3,4] and associated with propeller wake measurements related to hull interactions [5,6]. Although essential general propeller phenomena (tip vortices, wake evolution) are highlighted in these cases, recent experiments dedicated to (unsteady) aeronautical applications remain minimal. In contradiction to a low availability of experimental data, computational data flourish. However, due to the complexity of propeller flow (three-dimensionality, unsteadiness) simplifications in the calculations have to be made, such as modeling the propeller as an actuator disk, neglecting of viscosity [7], and difficulties in wake modeling [8]. Other problems are the distinction between numerical dissipation and turbulence decay [9] and the computational costs of performing 3-D unsteady propeller calculations. Although the performance of a propeller–wing combination is dictated by time-averaged forces [2], unsteady effects are related to a decrease in the section drag coefficient (when compared with a fully turbulent boundary layer) and are caused by a periodic alternation between a laminar and a

Presented as Paper 3810 at the 25th AIAA Applied Aerodynamics Conference, Miami, FL, 25–28 June 2007; received 7 August 2007; accepted for publication 12 September 2008.

*Research Scientist, Experimental Methods, Institute of Aerodynamics and Flow Technology, Bunsenstr. 10; eric.roosenboom@dlr.de. Member AIAA.

†Ph.D. Researcher, Experimental Methods, Institute of Aerodynamics and Flow Technology, Bunsenstr. 10.

‡Research Scientist, Experimental Methods, Institute of Aerodynamics and Flow Technology, Bunsenstr. 10.

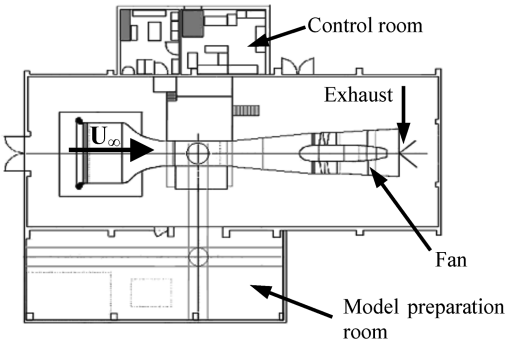

Fig. 1 Wind tunnel layout.

turbulent state of the wing boundary layer [10]. Increased propulsive efficiency leads to effects related to a high disk loading (i.e., the propeller thrust divided by the swept area of the propeller disk), in particular for propellers equipped with multiple blades. Such effects are apparent in the slipstream where propeller–wing interaction due to high swirl velocities alters the lift distribution over the wing, and thus alters the performance and behavior of the propeller and the wing [2]. The need to gain knowledge of the unsteady nature of propeller flow has lead to some recent investigations in unsteady phenomena occurring at propeller thrust reverse [11].

To address these problems found in numerical calculations and to investigate the unsteady and periodic events in propeller flow, experiments dedicated to aerospace applications are often asked for. Particle image velocimetry (PIV) is a suitable experimental technique for providing instantaneous and averaged velocity (and velocity-derived quantities) field data [12] and giving insight in the complex flow phenomena occurring in these particular flows. PIV has proven its applicability in industrial wind tunnels [13] and is capable of delivering velocity data with a high spatial resolution. These velocity data can then be used for an impression of the propeller–wing interference and velocity-derived values, such as vorticity and turbulent kinetic energy, to yield a complete description of the propeller–wing interaction. Moreover, when numerical data are available the PIV measurements can be used to validate CFD (computational fluid dynamics) codes. For such validations, of particular interest is the amount of numerical dissipation and the required resolution of vortices, because these will affect the computational time.

II. Experimental Setup

The experiments are performed in the low-speed wind tunnel (LSWT) facility in Bremen. The wind tunnel is an open-type Eiffel wind tunnel with a closed cross section with an area of 2.1×2.1 m and a contraction ratio of 4.82:1. The length of the test section is 4.45 m. The return circuit is ensured by placement within a large hall. A schematic layout is depicted in Fig. 1. The wind tunnel can be operated in the velocity range from 5 to 80 m/s and was kept constant in order to maintain a constant advance ratio of 0.79 (based on the propeller diameter and the number of revolutions per second, $n_p = 247$). The Reynolds number was roughly 1.25×10^6. The half-model is equipped with a clockwise and a counterclockwise propeller (eight blades each). The rotation is such that the inboard propeller rotates upwards at the fuselage. The half-model is connected to a turntable at the ceiling of the wind tunnel. The measurements are performed at different thrust coefficient values while maintaining an equal advance ratio. The blade pitch angle for the measurements at the lower thrust value will therefore be lower than the blade pitch angle at the higher thrust coefficient. The thrust (or thrust coefficient) is controlled by monitoring the online revolutions of the propeller. Optical access for the laser is provided through several glass windows on the sides of the test section; access for the CCD (charge-coupled device) cameras to the test section is provided through a window in the turntable in the floor of the wind tunnel. An image of the model in the wind tunnel is shown in Fig. 2. The model is painted with a mixture of black acrylic paint and Rhodamine 6G, a

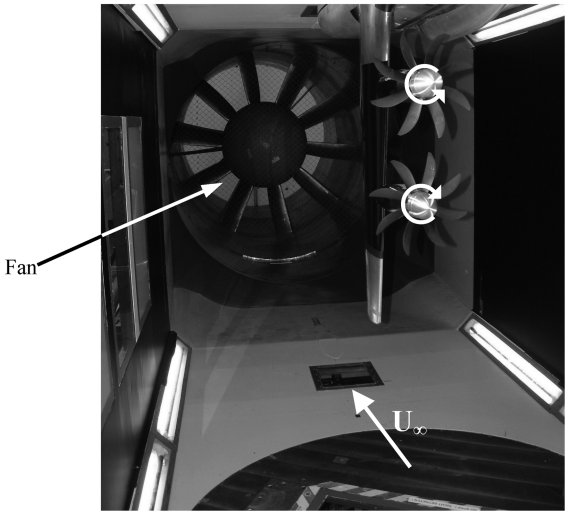

Fig. 2 Model in wind tunnel.

fluorescent paint, which absorbs light of wavelengths at 532 nm (i.e., the green laser light) and emits light at a slightly larger wavelength. The cameras are equipped with special color filters, such that only the green laser light is transmitted to the CCD-sensors. Reflections are significantly reduced by the application of this special mixture. In Fig. 2 the black painted region of the wing can be clearly identified.

Two double cavity BigSky CFR 200 Nd:YAG lasers with an output of 400 mJ per pulse were used to illuminate the seeding particles. The pulse duration of one pulse is approximately 9 ns, yielding a negligible angular displacement of 8×10^{-4} deg based on the rotation of the propeller. The time separation between two pulses is adjusted for respective measurements. Of course, such a displacement is necessary in order to discriminate particle displacement at high axial velocities and requires a trade-off between optimizing time separation and minimizing propeller rotations between pulses. The laser optics are connected to a traverse in order to allow a scanning in the spanwise direction over the wing (in the vertical direction), shown in Fig. 3. The imaging was performed with four PCO Sensicam CCD cameras [in a two-component (2C) arrangement], with a resolution of

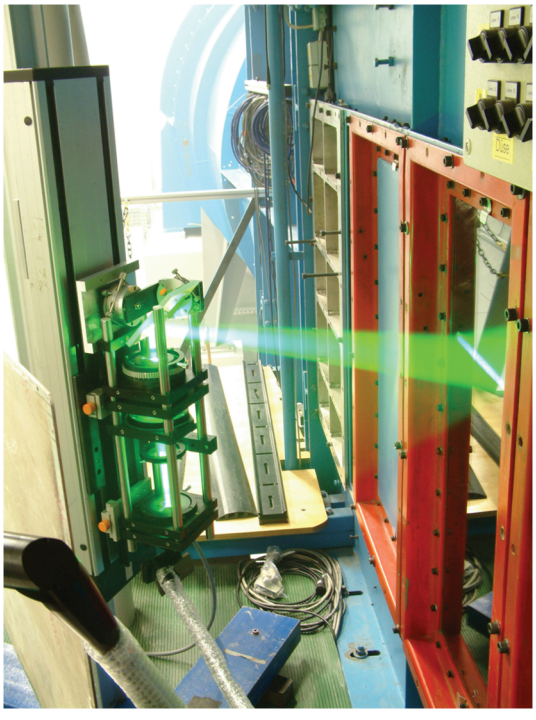

Fig. 3 Laser optics connected to traverse.

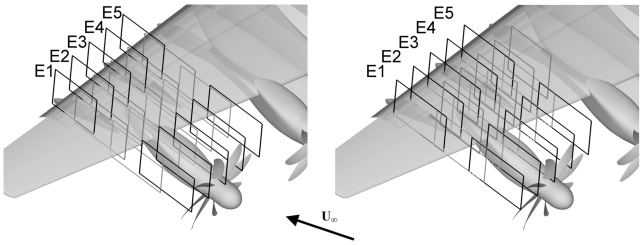

Fig. 4 Field of view of the four cameras, with the left showing arrangement 1 and the right showing arrangement 2 (indicated flow direction is valid for both arrangements). The symmetry plane of the propeller is depicted by E3.

1280×1040 pixel^2; the total resolution of the field of view with the four cameras is 5.4 megapixels and spans approximately 560 by 150 mm. The focal number was set to 2.8 in order to capture as much scattered particle light as possible. The cameras are connected to the turntable in the floor of the wind tunnel, so that their field of view remains the same when the model is placed at an angle of attack. In addition, the turntable can be traversed as well. The combination of simultaneously traversing the laser optics and the turntable, with the cameras, facilitates an easy means of performing the necessary calibrations and it also ensures that the field of view remains similar throughout the measurements. Aerosol generators, placed at the wind tunnel air intake, produced seeding particles with an average diameter of 1 μm and yielded a homogenous seeding in the wind tunnel test section [14]. All measurements are performed in a phase-locked sense, with respect to one single propeller blade. A transistor-transistor logic signal from the propeller is used as an input for a programmable sequencer to trigger the laser and to synchronize camera frames [15]. This system is capable of triggering up to 12 camera systems [16]. The acquired particle images are analyzed using the PIVview software [17], employing multigrid interrogation with image deformation. The following settings are used in the analysis: a final window size of 24×24 pixel^2, a step-size of 12 pixels (i.e., 50% window overlap). A spatial resolution of approximately 1.7 mm, in both directions, is reached in the final datasets. The layout of the final field of view is represented as in Fig. 4 for the two arrangements. Using the combined data of the four cameras, more than 43,000 instantaneous 2C vectors are available in each plane. A total number of 200 instantaneous image pairs (i.e., resulting vector fields) are acquired at each single measurement. It has to be noted that a linear interpolation of the results has been applied to the results being shown in this paper. The main reason to do so was to reduce minor artifacts at overlapping regions.

The arrangement of the cameras was changed during the measurements resulting in two different calibration views. Five slices in the spanwise direction were scanned, using the traverse, to obtain velocity vectors, at the outer diameters, half diameters, and the symmetry plane of the (outboard) propeller. These views are named E1 to E5, where E1 is the most outboard plane and E5 the most inboard plane. An overview of the layout of the field of view for the different cameras at the two calibrations is presented in Fig. 4. Parts where the field of view intersects with elements of the wing or propeller will be masked in the final datasets. The set of angles that were measured during the experiments are listed in Table 1. The angles of attack α_A and $\alpha_{B1,2}$ are within the linear part of the lift polar, and α_A is at cruise conditions. The lift coefficient has its maximum at the angles of attack $\alpha_{C1,2}$. The angles of attack deviate between the measurements of the no-thrust and thrust cases, as can be noted from this table. The reason for this is that with thrust ($C_T = 0.1$) a higher maximum lift coefficient can be reached due to the energy in the slipstream. Therefore, comparisons are made between the no-thrust ($C_T = 0$) and thrust ($C_T = 0.1$) cases at angles of attack at α_{C1} and α_{C2}. Only for one case (in the propeller symmetry plane), phase-shifted (phase-locked measurements at increments of 5° of a propeller passage) measurements have been performed. Despite the large amount of data that is available using a scanning PIV setup, it has to be noted that the results presented in this work focus only on the comparison between no-thrust and thrust conditions at two angles of attack and a description of the wake evolution of the phase-shifted results in the symmetry plane of the propeller (as indicated in Table 1).

Table 1 Measurement test matrix

Angle of attack, α	Planes	C_T	Results shown in plane
α_A	E1–E5	0.0	E3
α_A	E1–E5	0.1	E3
α_{B2}	E3	0.1	E3[a]
α_{C1}	E2–E5	0.0	E3
α_{C2}	E1–E5	0.1	E3

[a]Phase evolution

III. Results

The following results are presented for the measurements: phase-locked mean averaged velocity fields, contourplots of vorticity, and estimates of the turbulent kinetic energy. Also, for one particular experimental case with thrust, a measurement at different phase-shifts was performed. Generally PIV results are biased at the edges; therefore, the resulting four fields of views are merged into one single contour. This reduces artifacts caused at overlapping edge regions. In some results, there may be an optical mismatch between the propeller and data, but this is only due to the representation of the model. The several measurements are performed at slightly different phase angles in order to reduce reflections; the specific propeller position as depicted in the results therefore not does necessarily represent the actual propeller position.

A. Velocity

Approximately 43,000 instantaneous velocity vectors are obtained in the combined field of view of the four cameras. Contours of the averaged magnitude of the velocity (over 200 instantaneous realizations) in the symmetry plane are presented in Fig. 5 for two different angles of attack and the two thrust values. The influence of the angle of attack is apparent by comparing Fig. 5a with Fig. 5c and Fig. 5b with Fig. 5d respectively. For the no-thrust case the increase in angle of attack lowers the slipstream velocity over the wing. The tip vortices are equal for both cases. For the thrust case the tip vortices become less pronounced, and over the wing a region of separation starts to develop as the angle of attack is near the end of the linear part of the lift curve.

B. Vorticity

A comparison of the vortices at the tip of the propeller is made available by the vorticity plots in Fig. 6. The vorticity is determined as $\omega_y = \frac{\partial u}{\partial z} - \frac{\partial w}{\partial x}$ (in the current coordinate system) and represents the out-of-plane component of the vorticity vector. The tip vortices for the no-thrust cases remain indeed almost constant. Additionally, secondary vortices develop just above the boundary layer at a higher angle of attack (compare Fig. 6a with Fig. 6c). These vortices are generated due to instabilities of, and small rotations around, the shear line. This then leads to the break up of this shear line resulting in the secondary vortices. The boundary layer itself also increases in size due to the higher angle of attack. The notable difference between the two thrust cases is that the vortices have opposing values. The opposing values result from the fact that two different blade pitch angles are used during the measurements. Vorticity is defined as the summation of the normal derivatives of the horizontal and vertical velocity components. Because the horizontal velocity component is positive at both $C_T = 0$ and 0.1, the difference in vorticity contours is due to the vertical velocity component. Figure 7 indeed confirms that at the location of the vortices the w component is different. In fact, this difference is caused by the blade pitch angles required at these two thrust cases. At the higher thrust case, a higher blade pitch angle is used. The local effective (blade) angle of attack is thus also higher, whereas for the lower thrust case the local (blade) angle of attack is lower. This effect is even more enhanced due the acceleration of the

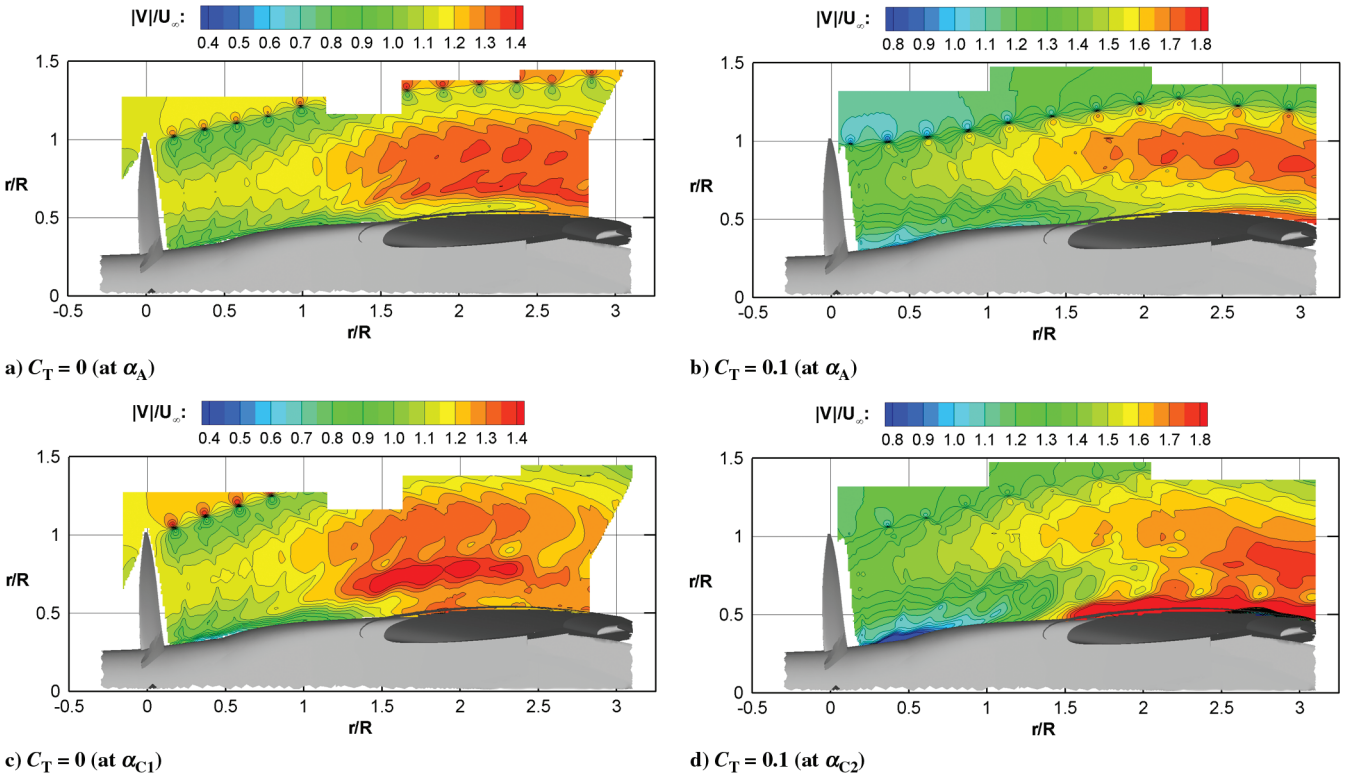

a) $C_T = 0$ (at α_A)

b) $C_T = 0.1$ (at α_A)

c) $C_T = 0$ (at α_{C1})

d) $C_T = 0.1$ (at α_{C2})

Fig. 5 Magnitude of velocity in the symmetry plane. (Refer to Table 1 for a definition of the angles.)

flow at the propeller disk. The more accelerated flow at the higher thrust case is capable of sustaining better in the propeller slipstream. This ultimately leads to the effect that the tip vortices at the no-thrust case precede the main slipstream profile, whereas at the thrust case the main slipstream profile is formed out of the tip vortices. The tip vortices at the zero thrust case more or less slow down the flow in the slipstream of the propeller. The vorticity profile for the thrust case is more pronounced (see Figs. 6b and 6d).

An increase of the angle of attack for the thrust case leads to the generation of vortices in the boundary layer. Howard et al. [10] describe an intermittent state of turbulence, for a laminar wing, where the flow over the wing goes from turbulent to laminar to turbulent and again back to laminar. Indeed, they conclude that this is due to the blade viscous wake. In the present results at the higher thrust case for the higher angle of attack shown in Fig. 6d, the secondary vortices, also present in Fig. 6b, are generated in the boundary layer as for

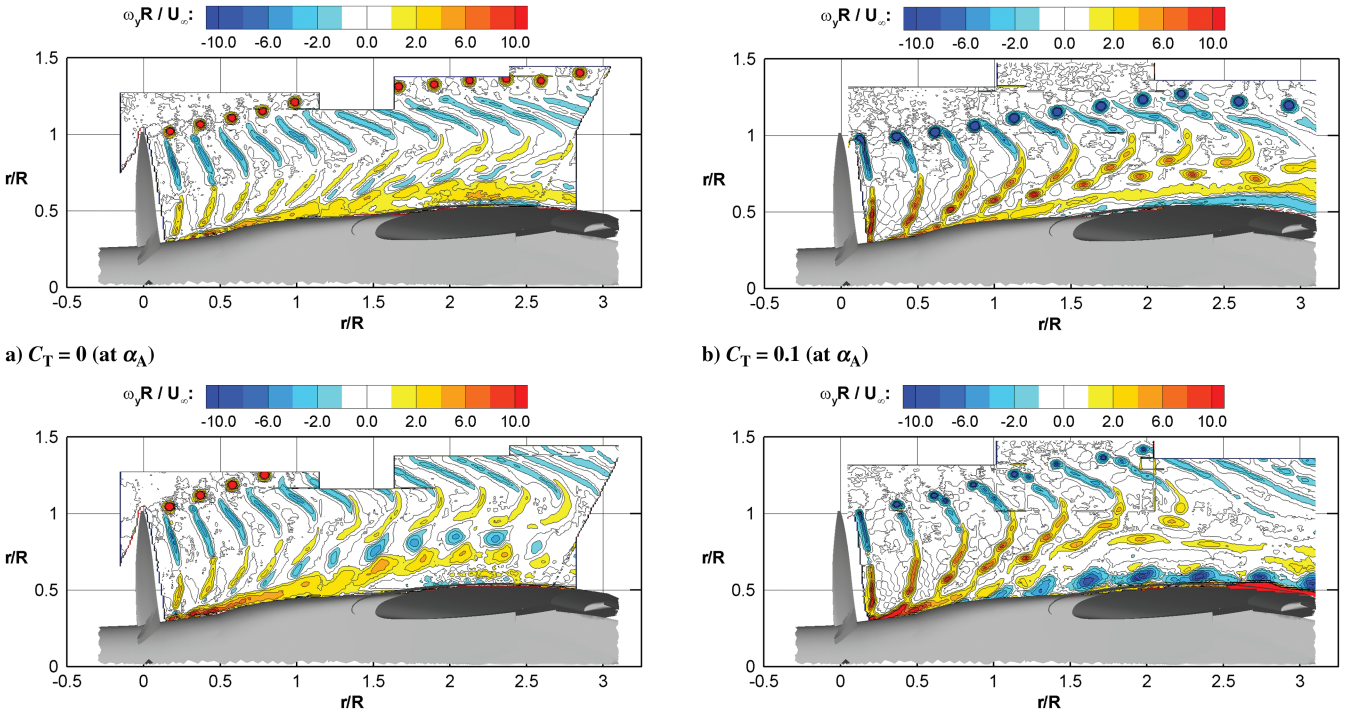

a) $C_T = 0$ (at α_A)

b) $C_T = 0.1$ (at α_A)

c) $C_T = 0$ (at α_{C1})

d) $C_T = 0.1$ (at α_{C2})

Fig. 6 Vorticity in the symmetry plane. (Refer to Table 1 for a definition of the angles.)

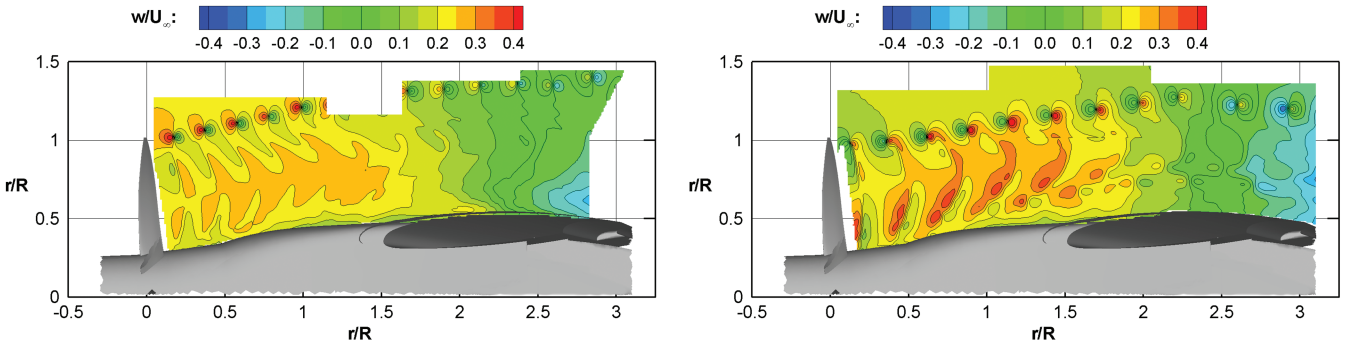

a) $C_T = 0$ (at α_A) b) $C_T = 0.1$ (at α_A)

Fig. 7 Vertical (w) velocity component. (Refer to Table 1 for a definition of the angles.)

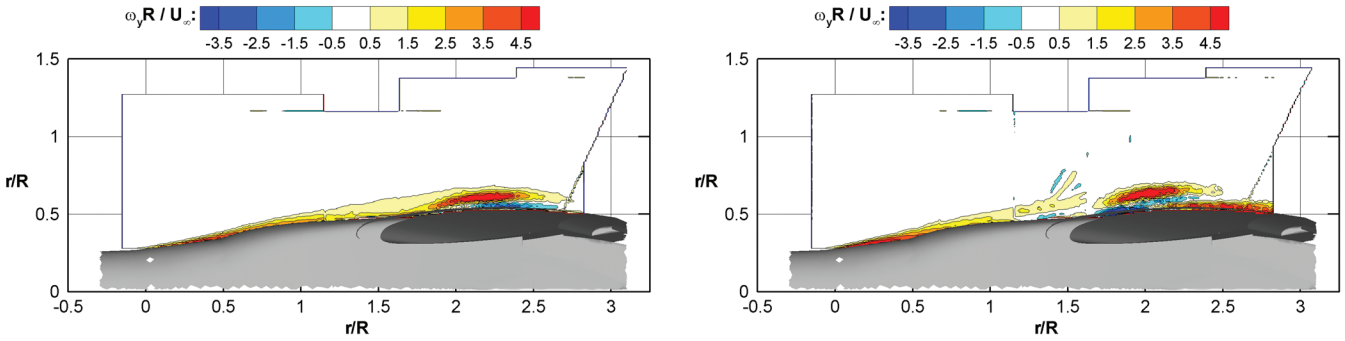

a) α_A b) α_{B2}

Fig. 8 Vorticity in the propeller-off case. (Refer to Table 1 for a definition of the angles.)

higher vortex strengths (i.e., thrust), and the higher velocities in the slipstream, the more capable the flow is of withstanding velocity fluctuations. It is assumed that the secondary vortices, induced by the nacelle, can be responsible for such events. Again, break up of the shear line is causing the secondary vortices, and due to the higher velocities at the thrust case, the secondary vortices are convected downstream. These boundary layer vortices then generate an intermittent flow pattern. As can be seen in the results at two propeller off-cases (Fig. 8) vorticity is induced by the nacelle. This vorticity has a negative value and is present in all datasets with propeller cases. At the propeller cases, this induced vorticity is "sliced" by the slipstream of the propeller, resulting in the blobs of vorticity ultimately leading to the effect of secondary vortices.

The flow separates due to the higher angle-of-attack and thrust values, the flow becomes turbulent, and the vortices are formed. The increased turbulence then enables reattachment of the boundary layer. Of course, these vortices move with the propeller rotation, and an intermittent fluctuating turbulent pattern is obtained. An estimate for separated flow can be obtained by the flow curvature [18], where separation is indicated with negative curvature (i.e., backflow). The flow curvature is defined as $\partial u/\partial z$ (i.e., the normal derivative of the horizontal velocity component). Figure 9 presents the flow curvature for the thrust case at the two angles of attack. At the lower angle of attack, the boundary layer of the flow over the wing is of a turbulent nature, and a confined separation region is present from the highest point of the wing (Fig. 9a). The intermittent separated regions in the boundary layer at higher angles of attack are confirmed with the curvature in Fig. 9b. Alternated regions of positive and negative curvature appear, causing periodic events in the boundary layer.

C. Turbulent Kinetic Energy

Other features of this type of flow can be addressed by considering the turbulent kinetic energy of the velocity fluctuations K. This quantity is defined as

$$K = 0.5(\overline{u'u'} + \overline{v'v'} + \overline{w'w'}) \tag{1}$$

Turbulent kinetic energy can be regarded as a measure for "turbulence conservation" and is useful in a description of time-averaged datasets, such as the PIV datasets here. The next graphs

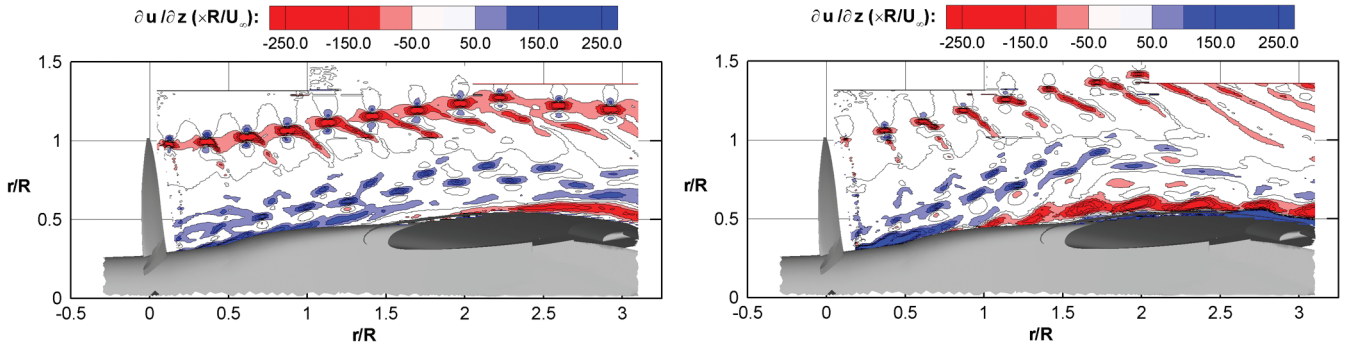

a) $C_T = 0.1$ (at α_A) b) $C_T = 0.1$ (at α_{C2})

Fig. 9 Flow curvature in the symmetry plane. (Refer to Table 1 for a definition of the angles.)

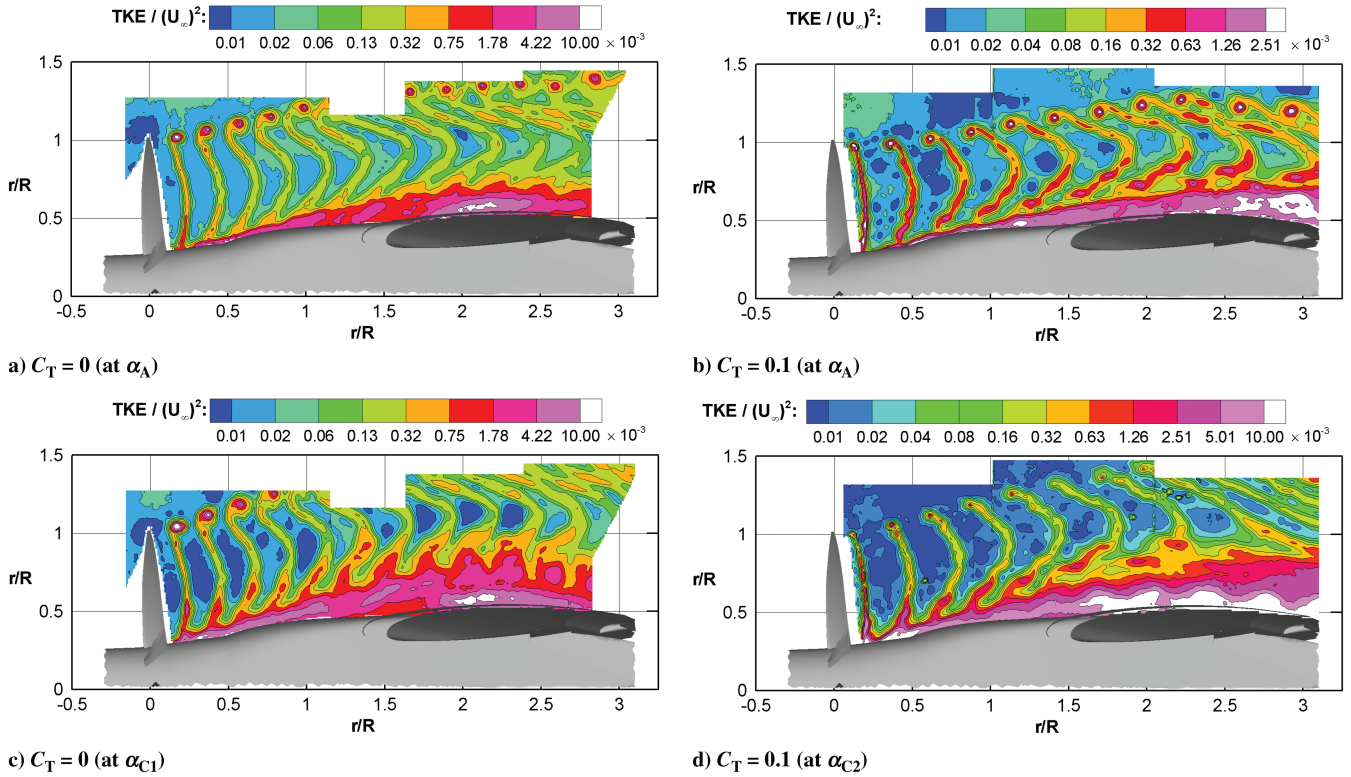

Fig. 10 Turbulent kinetic energy distribution (with exponential color map) in the symmetry plane. Note that b) has two levels less than other graphs. (Refer to Table 1 for a definition of the angles.)

show the features of this quantity in the symmetry plane, shown in Fig. 10. An exponential color map is used in order to account for the several features found in the results; its values are depicted in Fig. 11. Comparing again the no-thrust and thrust cases, it is confirmed that the energy production within the tip vortices are stronger for the no-thrust case. Moreover, the general value of the energy production is lower for the thrust case. The larger boundary layer at higher angles of attack is confirmed by the higher turbulent kinetic energy in the boundary layer. For the no-thrust case, the production of the secondary vortices is identified by the turbulent kinetic energy. Tip vortices are convected quasi downstream of each corresponding shear line for the no-thrust case, whereas the tip vortices at the thrust case precede the corresponding shear line. This is due to the sense of rotation and roll up of these vortices.

D. Phase-Shifted Results in Propeller Symmetry Plane

In the center cross section (E3), the symmetry plane of the propeller, several phase-shifted measurements were performed at an angle of attack of α_{B2}; this angle lies between α_A and α_{C2}, the angles in Figs. 6a and 6d. This angle is chosen because it allows a future comparison with numerical data. The measurements were performed with a difference in phase angle of 5 deg in order to investigate the evolution of the vortices in the propeller wake. During one blade-to-blade rotation (0 to 40 deg) instants are presented in Fig. 12. Only instants at a phase angle difference of 10 deg are presented, as the intermediate instants are intrinsically similar. The measurements were triggered with respect to one blade; the initial phase angle with respect to this blade is 15.1 deg (in propeller rotation direction). The respective vorticity patterns are averaged over 200 PIV recordings at the corresponding phase angle. The general pattern of the vorticity remains identical at the several phases. Nevertheless, small differences occur for the blade-to-blade pattern of the vorticity. In particular, when focusing on the tip vortices, a deviating pattern is present. Although it can be argued that these patterns occur for different phases of the vortex production, it is interesting to note that this pattern is *not* changing at the individual phases. Two plausible explanations could be that the propeller blades have small deviations or that vorticity is formed due to a combination of twist and bending on the specific blades. For this angle of attack, similar vortical structures appear in the boundary layer at these phase-averaged results and move downstream with the increasing phase angles. It is assumed that these boundary layer vortices cause periodic pressure fluctuations and/or wall shear stress fluctuations in the boundary layer of the nacelle. Although these periodic events on their own might not be favorable, the lift will benefit from the generated increased velocities over the wing.

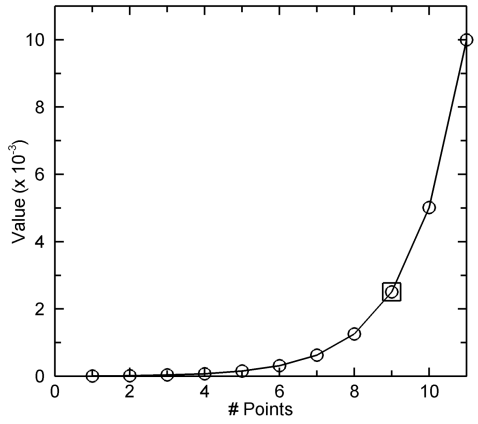

Fig. 11 Values used for the exponential color map in Fig. 10. Figure 10c uses values until point 9 (indicated with square symbol).

IV. Conclusions

The still-increasing oil prices have lead to a revived interest in propeller experiments, as turboprops offer several advantages over regular turbofans (i.e., fuel efficiency). Only marginal experimental propeller data are available. The present investigation focuses on the investigation of the slipstream behind the outboard propeller of a half model equipped with two propellers with opposing rotation directions. The slipstream is analyzed using two-component particle image velocimetry in an industrial wind tunnel. The cameras were

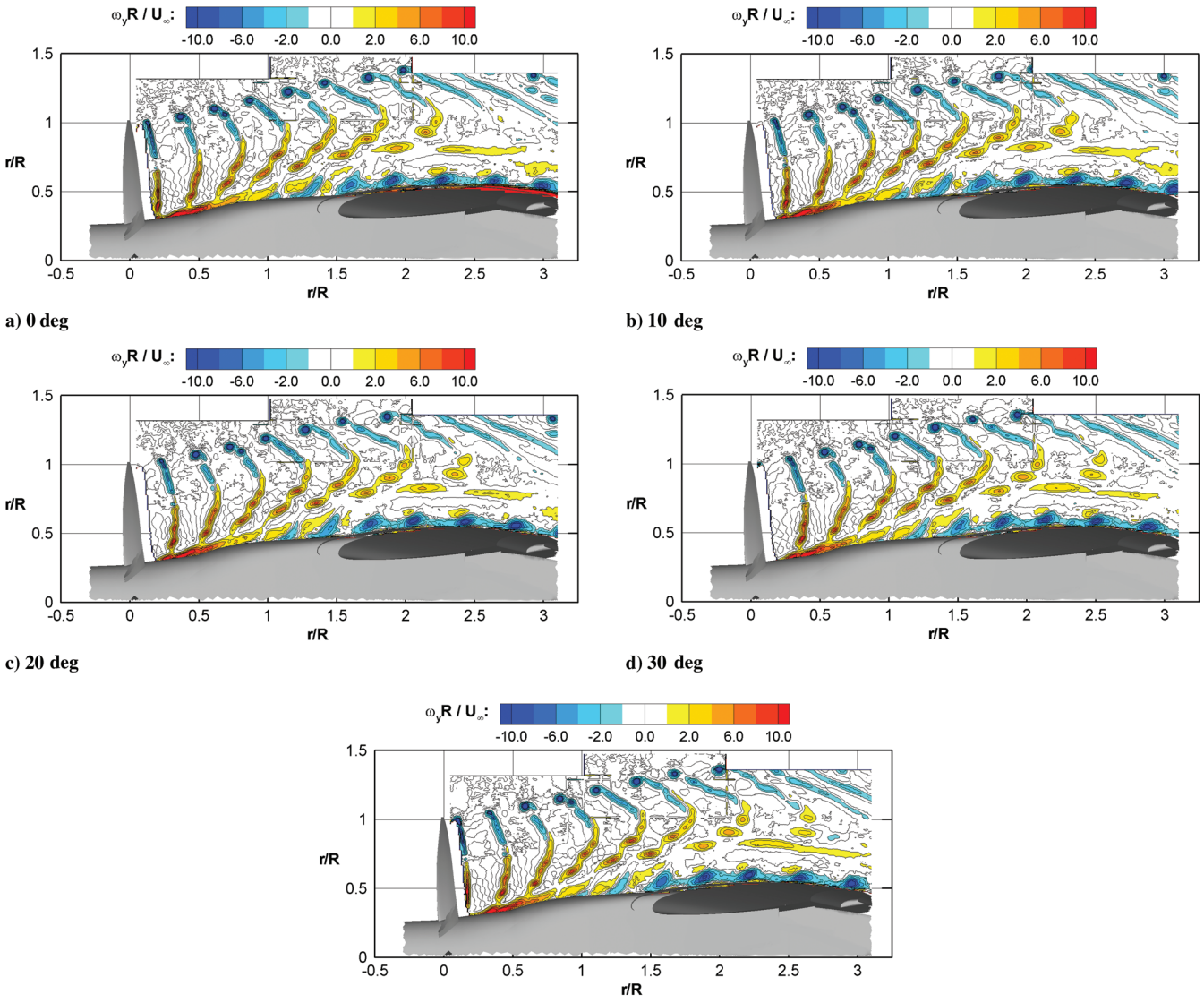

Fig. 12 Phases of vortex development in blade-to-blade movement in the symmetry plane at α_{B2}, with the initial key blade phase position of 15.1 deg in propeller rotation. (Refer to Table 1 for a definition of the angles.)

connected to the wind tunnel turntable, so that the field of view remained the same when the wind tunnel model was placed at the angle of attack. By traversing the laser optics and the cameras simultaneously, it was possible to scan several spanwise positions within the propeller disk area. The use of the traverse offered the possibility of fast calibrations. The detailed visualization of complex flows, such as a periodic and unsteady propeller flow, is necessary to understand the complex propeller flow phenomena. Propeller–wing interactions are dependent on the periodic events in the slipstream and require an investigation in order to recognize the extent thereof. Additionally, detailed experimental slipstream investigations are necessary for numerical simulations. At all measurement points, 200 instantaneous velocity (two-component) vector fields were acquired in the phase-locked sense. A signal of one propeller blade was used to trigger the laser and cameras. A no-thrust ($C_T = 0$) and thrust ($C_T = 0.1$) case are compared at two different angles of attack, with the lower angle of attack within the linear part of the lift curve and the higher angle of attack near the end of the linear part of the lift curve. The evolution of the tip vortices is captured for the several measurements. Additionally, it is found that secondary boundary layer vortices are formed in the slipstream. These secondary vortices move with the blade wake (i.e., blade passage) and cause regions of periodic attached and separated flow. These vortices are most probably caused by the induced vorticity around the nacelle. With respect to CFD validations, it can be mentioned that the observed periodical phenomena in the nacelle require significant awareness for accurate numerical simulations due to possible numerical dissipation effects that need to be distinguished from (or may influence) these periodic events.

Acknowledgments

The measurement campaign was performed as part of a collaboration with Airbus and was conducted within the IHK-HICON German research project. The authors gratefully acknowledge Airbus for the opportunity to publish the results and in particular, Klaus-Peter Neitzke for his valuable comments on this paper.

References

[1] Ruijgrok, G. J. J., "Propeller Performance," *Elements of Airplane Performance*, Delft University Press, Delft, The Netherlands, 1996, Chap. 7.

[2] Veldhuis, L. L. M., "Propeller Wing Aerodynamic Interference," Ph.D. Dissertation, Delft University of Technology, Delft, The Netherlands, 2005.

[3] Cotroni, A., Di Felice, F., Romano, G. P., and Elefante, M., "Investigation of the Near Wake of a Propeller Using Particle Image

Velocimetry," *Experiments in Fluids*, Vol. 29, No. 7, 2000, pp. S227–S236.
doi:10.1007/s003480070025

[4] Lee, S. J., Paik, B. G., Yoon, J. H., and Lee, C. M., "Three-Component Velocity Field Measurements of Propeller Wake Using a Stereoscopic PIV Technique," *Experiments in Fluids*, Vol. 36, No. 4, 2004, pp. 575–585.
doi:10.1007/s00348-003-0699-5

[5] Paik, B. G., Lee, C. M., and Lee, S. J., "PIV Analysis of Flow Around a Container Ship Model with a Rotating Propeller," *Experiments in Fluids*, Vol. 36, No. 6, 2004, pp. 833–846.
doi:10.1007/s00348-003-0765-z

[6] Calgano, G., Di Felice, F., Felli, M., and Pereira, F., "Propeller Wake Analysis Behind a Ship by Stereo PIV," *24th Symposium on Naval Hydrodynamics*, National Academy Press, Washington, D.C., 2003, pp. 789–805.

[7] Bousquet, J.-M., and Gardarein, P., "Improvements on Computations of High Speed Propeller Unsteady Aerodynamics," *Aerospace Science and Technology*, Vol. 7, No. 6, 2003, pp. 465–472.
doi:10.1016/S1270-9638(03)00046-4

[8] Chiaramonte, J.-Y., Favier, D., Maresca, C., and Agnes, A., "Unsteady Interactional Effects Between a Propeller and a Fixed Wing," *9th Applied Aerodynamics Conference*, AIAA Paper 91-3231, Sept. 1991.

[9] Stuermer, A., Rakowitz, M., "Unsteady Simulation of a Transport Aircraft Using MEGAFLOW," *Flow Induced Unsteady Loads and the Impact on Military Applications*, RTO-MP-AVT-123 AC/323(AVT-123)TP/92, NATO, 2005.

[10] Howard, R. M., Miley, S. J., and Holmes, B. J., "An Investigation of the Effects of the Propeller Slipstream on a Laminar Wing Boundary Layer," Society of Automotive Engineers Technical Paper 850859, 1985.

[11] Roosenboom, E. W. M., and Schröder, A., "Propeller Thrust Reverse," *7th International Symposium on Particle Image Velocimetry*, Rome, Italy, Sept. 2007.

[12] Raffel, M., Willert, C. E., Wereley, S. T., and Kompenhans, J., *Particle Image Velocimetry: A Practical Guide*, 2nd ed., Springer–Verlag, Berlin, 2007, Chap. 2.

[13] Stanislas, M., Kompenhans, J., and Westerweel, J., *Particle Image Velocimetry: Progress Towards Industrial Application*, Kluwer Academic, Norwell, MA, 2000.

[14] Kähler, C. J., Sammler, B., and Kompenhans, J., "Generation and Control of Tracer Particles for Optical Flow Investigations in Air," *Experiments in Fluids*, Vol. 33, No. 6, 2002, pp. 736–742.doi:10.1007/s00348-002-0492-x

[15] Stasicki, B., Ehrenfried, K., Dieterle, L., Ludwikowski, L., and Raffel, M., "Advanced Synchronization Techniques for Complex Flow Field Investigations by Means of PIV," *Proceedings of the 4th International Symposium on PIV*, Paper 1188, Göttingen, Germany, Sept. 2001.

[16] Von Carmer, C. F., Konrath, R., Schröder, A., and Monnier, J.-C., "Identification of Vortex Pairs in Aircraft Wakes from Sectional Velocity Data," *Experiments in Fluids*, Vol. 44, No. 3, 2008, pp. 367–380.doi:10.1007/s00348-007-0450-8

[17] Willert, C., "PIVview 2C/3C User Manual Version 2.3," http://www.pivtec.com [retrieved 13 Sept. 2006].

[18] White, F. M., *Viscous Fluid Flow*, 2nd ed., McGraw–Hill, New York, 1991.